Study on Chemical Bond Dissociation and the Removal of Oxygen-Containing Functional Groups of Low-Rank Coal during Hydrothermal Carbonization: DFT Calculations

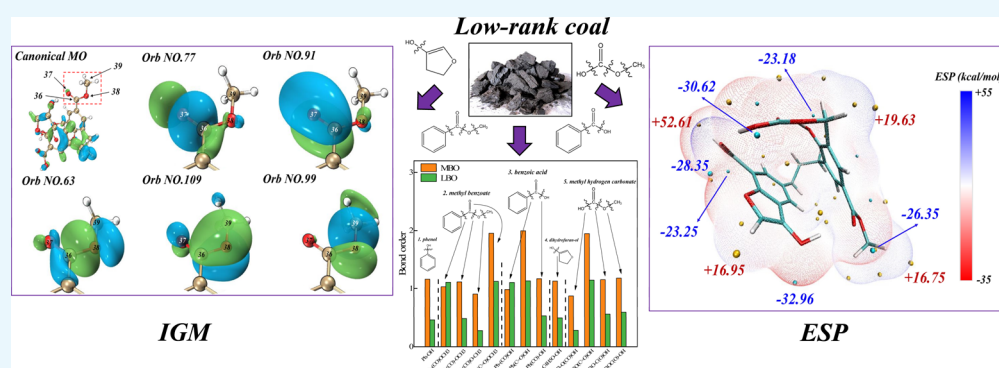Han Dang, Guangwei Wang,* Chunmei Yu, Xiaojun Ning,* Jianliang Zhang, Nan Zhang, Yi Gao, Runsheng Xu,* and Chuan Wang

ACCESS | Metrics & More | Article Recommendations

ABSTRACT: The molecular structure model of lignite was constructed, and the dissociation and removal mechanism of different C−O bonds and oxygen-containing functional groups was investigated using density functional theory (DFT) calculations. First, the bond order and bond dissociation enthalpy (BDE) were analyzed to predict the strength of different chemical bonds, and differences in the BDE and bond order were related to the difference in the fragment structure and electronic effects. The first group to break during hydrothermal carbonization (HTC) is the methyl of $Ph(CO)O−CH_3$, followed by the C−O of $CH_3−OC(O)OH$; the hydroxyl in Ph−OH is the most thermally stable group, followed by the hydroxyl in $CH_3OC(O)−OH$. In addition, the orbital localization analysis has also been carried out. All three chemical bonds of $Ph(CO)OCH_3$ show the characteristics of σ bond, while $Ph(C=O)OCH_3$ and $Ph(CO)−OCH_3$ with the Mayer bond order (MBO) greater than 1 also contains certain π bond characteristics. The lignite van der Waals (vdW) surface electrostatic potential (ESP) was constructed and visualized, and the results showed that the oxygen-containing functional groups mainly contributed to the area with a large absolute ESP. Finally, weak interactions between water molecules and lignite at different sites were described by independent gradient model (IGM) analysis. Models A, B, and E formed weak interactions with the hydrogen bond as the main force; model E showed the weakest hydrogen bond, while model C showed van der Waals interaction as the dominant force. In addition, some steric effect was also observed in model D.

1. INTRODUCTION

Coal is one of the important fuels in blast furnace ironmaking, and the use of pulverized coal injection instead of coke in a blast furnace can improve the furnace condition and has better economic and social benefits, which is in line with the construction and development goal of the low carbon economy. However, high-rank coal resources in China are seriously inadequate. According to the statistics of China's mineral resources report in 2018, the proven reserves of coal in 2017 are 166.673 billion tons,[1] of which low-rank coal reserves account for more than 50% of the country's total coal reserves. The most typical low-rank coal is lignite, which accounts for 12% of the total coal reserves in China. In the foreseeable future, coal will still occupy an important position as primary energy in China. With the continuous mining and consumption of high-rank coal, low-rank coal with abundant reserves has entered the field of vision of researchers. However, low-rank coal has high moisture content and contains a large number of carboxyl, hydroxyl, and other oxygen-containing functional groups.[2] These groups have
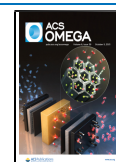
strong hydrophilicity, which makes a large amount of water firmly bound to the surface of the low-rank coal, which limits the large-scale use of low-rank coal in the industrial field. Hydrothermal carbonization (HTC) can irreversibly remove a large amount of internal water from the low-rank coal and has the functions of increasing the heating value, carbonization, and surface modification, and so, it is a feasible method to clean and efficiently utilize the low-rank coal.[3]

In the process of HTC, the change in physical and chemical properties of low-rank coal, the removal of oxygen-containing functional groups, and moisture are all key issues that need to be further explored.[4] The structure of coal is very complicated; considering lignite as an example, many scholars have conducted long-term research on the structure of lignite and many structural models have been conceived.[5] There are a large number of hydrogen bonds and van der Waals (vdW) and other weak interactions in lignite molecules, which makes lignite hydrophilic and is also an important reason for the high moisture content of low-rank coals.[6,7] The influence of HTC on the oxygen-containing functional groups in lignite molecules has been studied by many scholars. Wu[8,9] performed HTC of lignite at 200, 250, 280, 300, and 320 °C to explore the changes in the content of free water and bound water. There are 0.119 g/g bound water and 0.132 g/g free water in raw coal. After HTC at different temperatures, the content of free water and bound water drops to 0.097 and 0.073, 0.079 and 0.061, 0.056 and 0.044, 0.042 and 0.035, and 0.028 and 0.033 g/g, respectively. The results showed that HTC can remove free water and bound water in lignite. In addition, the NMR method was used to compare lignite raw coal and 300 °C HTC treatment coal, and the results showed that the content of carboxyl groups, ethers, and C=O bonds decreased by more than 50%, indicating that HTC can promote the reduction of oxygen content in molecules. Feng[10] analyzed the lignite after HTC using the Fourier transform infrared (FTIR) method and found that the ratio of hydroxyl to aromatic carbon decreased from 2.8 to 1.1, and the ratio of carboxyl to aromatic carbon decreased from 0.5 to 0.2, but the decrease of carboxyl groups was not significant. This may be because the carboxyl group mainly belongs to the aliphatic chain acid functional group, while the hydroxyl group mainly belongs to the aromatic functional group, and the aliphatic chain is easier to break during the upgrade process. Man[11] carried out HTC of lignite and explored the changes in the ratio of C—O bond to aromatic carbon and the ratio of carboxyl to aromatic carbon at 200, 240, and 280 °C. The results showed that the ratios of C—O bond to aromatic carbon were 0.229, 0.167, and 0.048 with increasing temperature, and the ratios of carboxyl to aromatic carbon were 0.597, 0.520, and 0.454 with increasing temperature, indicating that the content of oxygen-containing functional groups and C—O chemical bonds showed a declining trend in HTC. Wan[12] performed HTC on three lignites of Shengli (SL), Canada lignite (CAN), and Xiaolongtan (XLT) at 300 °C, and found that the reduction of —COOH and —OH was the largest. By analyzing the ratio of carboxyl to aromatic carbon and the ratio of hydroxyl to aromatic carbon, the results show that the decreases in the ratios of carboxyl to aromatic carbon are 0.505, 0.216, and 0.335, respectively. The decreases in the ratios of the hydroxyl to aromatic carbon are 4.277, 0.424, and 1.438, respectively. While FTIR, Raman, and NMR methods have been used to study oxygen-containing functional groups in lignite, there are few theoretical studies describing the changes of oxygen-containing groups in HTC at the molecular level. Therefore, it is necessary

to conduct more in-depth research from the theoretical aspect.[13−16]

In this study, density functional theory (DFT) combined with wave function analysis was used to study the breaking mechanism of chemical bonds in lignite molecules at a molecular level, and the bond dissociation enthalpy (BDE) and bond order were discussed. The contribution of molecular orbitals (MO) to bond formation was studied using orbital localization analysis. The molecular surface electrostatic potential (ESP) model and the water-coal adsorption model were constructed, which theoretically described the weak interaction between water molecules and lignite and explained the reason for the high moisture in lignite.

2. RESULTS AND DISCUSSION

2.1. Bond Order and BDE Analysis. The Mayer bond order (MBO) and Laplacian bond order (LBO) were used to analyze the bond order of some C—O bonds and the bonds linking oxygen-containing functional groups in the lignite molecule; the results are shown in Table 1. It can be found

Table 1. MBO and LBO Values of C—O and C—C Bonds[a]

no.	chemical groups	bond	MBO	LBO
1	phenolic hydroxyl	Ph—OH	1.162	0.462
2	ester 1	Ph—(CO)OCH$_3$	1.032	1.109
2	ester 1	Ph(CO)—OCH$_3$	1.116	0.486
2	ester 1	Ph(CO)O—CH$_3$	0.904	0.279
2	ester 1	Ph(C=O)OCH$_3$	1.952	1.124
3	carboxyl	Ph—(CO)OH	0.983	1.105
3	carboxyl	Ph(C=O)OH	1.995	1.133
3	carboxyl	Ph(CO)—OH	1.170	0.530
4	hydroxyl	C$_4$H$_5$O—OH	1.129	0.497
5	ester 2	CH$_3$—O(CO)OH	0.872	0.283
5	ester 2	CH$_3$O(C=O)OH	1.947	1.147
5	ester 2	CH$_3$O—C(O)OH	1.154	0.560
5	ester 2	CH$_3$OC(O)—OH	1.181	0.592

[a]Ph represents phenyl.

that the MBO of C=O and C—O is, respectively, about 2 and 1, which is very consistent with the theoretical bond order value. As the LBO only reflects the covalent part between atoms and it is significantly smaller than the MBO,[33] the stronger the polarity of the chemical bond, the smaller the value of LBO. The bonds linking oxygen-containing functional groups to lignite are similar in value and both are about 1. However, for different types of C—O bonds, the MBO increases with the increase of the LBO value,[34] as shown in Figure 1.

According to the value of the bond order and the bond type, these bonds can be divided into the following four categories:

(A) C—O bonds in Ph(CO)O—CH$_3$ and CH$_3$—O(CO)OH. Both of them have strong polarity, which causes their MBOs to be significantly lower than 1, and are 0.904 and 0.872, respectively. Polarity also had a significant effect on the LBO, resulting in their LBOs of 0.279 and 0.283, respectively. According to Liu,[9] this type of C—O has poor thermal stability and it is easy to dissociate to generate CO and CO$_2$ in the hydrothermal reaction.

(B) C—O bonds in Ph—OH, Ph(CO)—OCH$_3$, Ph(CO)—OH, C$_4$H$_5$O—OH, CH$_3$O—C(O)OH, and CH$_3$OC(O)—OH. The thermal stability of this type of chemical bond is stronger than that of type A, and their MBOs are 1.162,
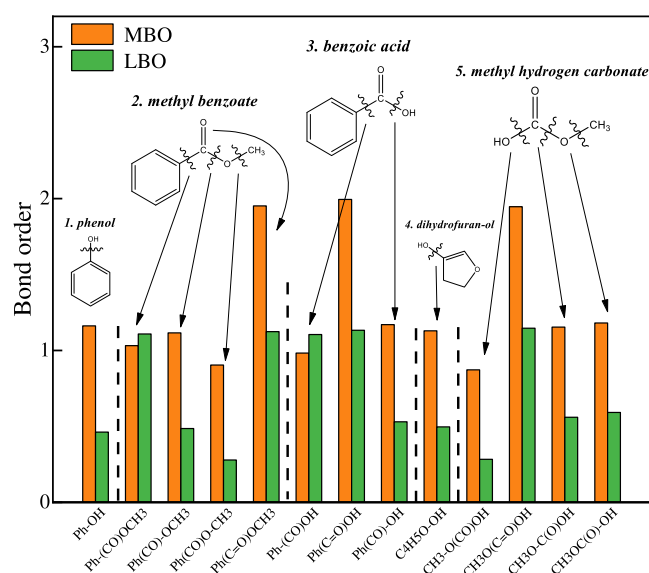
Figure 1. LBO and MBO values of different bonds.

1.116, 1.170, 1.129, 1.154, and 1.181, and their LBOs are 0.462, 0.486, 0.530, 0.497, 0.560, and 0.592, respectively. It can be seen that compared with the fragment without a stable structure, the bond order of the fragment with a stable structure is higher, and the closer the C−O bond is to the benzene ring, the less likely it is to dissociate.

(C) C−C bonds in Ph−(CO)OCH$_3$ and Ph−(CO)OH. Since the C−C bond is a covalent bond, the MBO and LBO are not significantly different in values. As can be seen from Table 1, the MBOs of C−C in Ph−(CO)OCH$_3$ and Ph−(CO)OH are 1.032 and 0.983, while LBOs are 1.109 and 1.105. Mo[35] pointed out that the closer to the aromatic structure, the more stable the chemical bond is, which also verified that HTC would lead to the structure removal of unstable small molecules, resulting in the aromatization of the whole system.

(D) C=O bonds in Ph(C=O)OCH$_3$ and CH$_3$O(C=O)OH. Due to the polarity of C=O, the MBO and LBO also differ greatly. Their MBO values are 1.995 and 1.947, and LBO values are 1.113 and 1.147, respectively. Therefore, this type of chemical bond is the most difficult to dissociate in the hydrothermal process.

Wu[8] pointed out that in the same chemical environment, the BDE of small molecules can well predict the corresponding bond strength of large molecules. According to his research, varied temperatures and pressures will affect the thermodynamic enthalpy values of molecules. Therefore, the change in the C−O bond BDE of CH$_3$O−CH$_3$ under constant temperature and differential pressure (25 °C, 1 atm) and under the temperature and pressure conditions of HTC was first studied by Wu. The results showed that the difference of the BDE at 25 °C and 90 atm is only 0.74 kcal/mol, compared with that at 300 °C and 90 atm. The electron energy molecules contribute most of the thermodynamic enthalpy in molecules, while the vibration and translation of molecules affected by temperature and pressure contribute less than the electron energy. Therefore, the influence of temperature and pressure on BDE values is very little and can be ignored.

The BDE values of different C−O bonds and C−C bonds connecting oxygen-containing functional groups are shown in

Table 2. According to the results of bond order analysis, C−O and C−C bonds were divided into four categories:

Table 2. BDE Values of C−O and C−C Bonds[a]

no.	chemical groups	bond	BDE (kcal/mol)
1	phenolic hydroxyl	Ph−OH[a]	115.04
2	ester 1	Ph−(CO)OCH$_3$	112.15
2	ester 1	Ph(CO)−OCH$_3$	102.51
2	ester 1	Ph(CO)O−CH$_3$	88.94
3	carboxyl	Ph−(CO)OH	112.70
3	carboxyl	Ph(CO)−OH	111.14
4	hydroxyl	C$_4$H$_5$O−OH	112.91
5	ester 2	CH$_3$−OC(O)OH	89.32
5	ester 2	CH$_3$O−C(O)OH	105.36
5	ester 2	CH$_3$OC(O)−OH	113.39

[a]Ph represents phenyl.

(A) MBOs of Ph(CO)O−CH$_3$ and CH$_3$−OC(O)OH were the lowest and their corresponding BDE values also belong to the smallest category, which are 88.94 and 89.32 kcal/mol, respectively. This may be due to the polarity between C−O bonds and the fracture trend is more obvious in the HTC process, which can verify that HTC has the function of removing the volatile matter.[36]

(B) MBOs of the C−O bonds were greater than 1, and their BDE values were greater than 100 kcal/mol. For partial chemical bonds, there is a linear relationship between the MBO and BDE. For example, the C−O bonds in Ph(CO)−OCH$_3$, CH$_3$O−C(O)OH, Ph(CO)−OH, and CH$_3$OC(O)−OH have MBOs of 1.116, 1.154, 1.170, and 1.181, respectively, and their BDE values were 102.51, 105.36, 111.14, and 113.39 kcal/mol, respectively. Ge[37] carried out a HTC upgrading treatment for Chinese low-rank coal, and found that the C/O atomic ratio of the samples after HTC decreased, which was consistent with the results of this study.

(C) The BDE values of C−C bonds were greater than most C−O bonds, and the values of both were above 110 kcal/mol. This may be because the C−C bond is a covalent bond and the shared electron pair of the two does not shift. Therefore, the thermal stability of these two C−C bonds during HTC is second only to the C=O bonds and the C−O bonds in Ph−OH, C$_4$H$_5$O−OH, and CH$_3$OC-(O)−OH.[38]

(D) The C=O bond has the highest MBO and is the most difficult to break during HTC. As can be seen from Table 2, the MBO and BDE have a good correspondence; the smaller the MBO, the smaller is the BDE and the worse is the thermal stability of the chemical bond in HTC.[39]

In addition, the differences in the bond order and BDE can also be explained by electronic effects and structural differences, as shown in Figure 2. The common electronic effects can be divided into the following categories: (1) field effect, which refers to the effect of substituents on the reaction center at the other end of the bond; (2) conjugation effect, which is generally an effect in the distribution of π electrons in the system changes due to the mutual influence between atoms; (3) induction effect, which is the effect of different polarities (electronegativity) of atoms or groups in molecules that causes the bonding electron cloud to move in a certain direction along the atomic chain. The induction effect generally exists between each fragment.
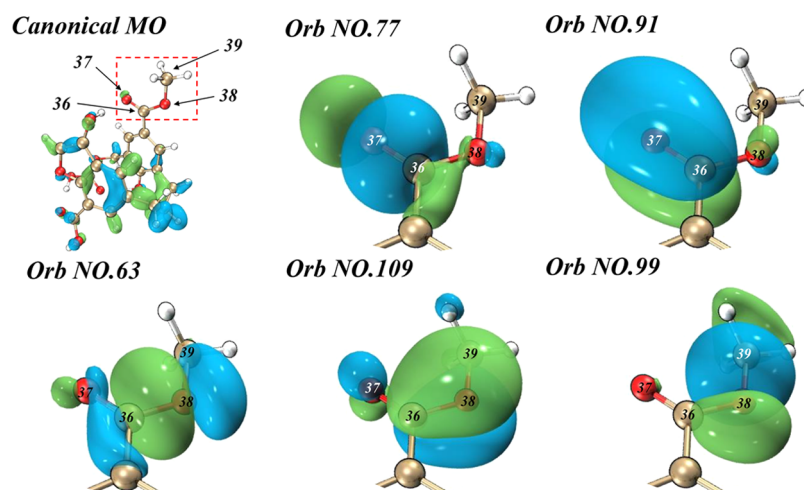
Figure 2. Canonical molecular orbitals (CMOs) and localized molecular orbitals (LMOs).

Considering fragments 1 and 4 as an example, the presence of −OH with large polarity leads to uneven distribution of the electric field of groups connected with −OH, which makes electrons shift toward the −OH end resulting in the bond order of C−O not equal to the theoretical value. The difference in the fragment structure is also the reason for the difference in values. The −OH of fragment 1 is connected to the benzene ring, which has the conjugated large π bond distributed in the whole system, and the whole system is in the same plane, which is relatively stable. In fragment 4, the oxygen-containing pentagonal furan structure is not in the same plane due to its structural tension and its energy is higher than that of the benzene ring. Therefore, its electron distribution is more susceptible to the influence of the induction effect, which also leads to the LBO and BDE of Ph−OH greater than that of C_4H_5O−OH. In the same fragment, the closer the bond is to the stable structure, the larger the bond order is.[35] Considering fragment 2 as an example, the distance between the C−O of Ph(CO)O−CH$_3$ and the benzene ring is larger than that between the C−O of Ph(CO)−OCH$_3$ and the benzene ring; so the MBO of the former is 0.904, while the MBO of the latter is 1.116, and the BDE followed the same trend. In fragment 5, CH$_3$−O(CO)OH is farthest from the C=O bond, while CH$_3$O−C(O)OH and CH$_3$OC(O)−OH are distributed on both sides of the C=O bond. Due to the influence of the −CH$_3$ induction effect, the electron was shifted, so the C−O bond order of CH$_3$O−C(O)OH was smaller than that of CH$_3$OC(O)−OH and the MBO and BDE of the three C−O followed the order CH$_3$OC(O)−OH > CH$_3$O−C(O)OH > CH$_3$−O(CO)OH.

In summary, the first group to break is the methyl of Ph(CO)O−CH$_3$, followed by the C−O of CH$_3$−OC(O)OH in HTC. The hydroxyl in Ph−OH is the most thermally stable group, followed by the hydroxyl in CH$_3$OC(O)−OH. The mechanism of removal of different chemical bonds and functional groups during HTC is clarified using quantum chemical calculations.

2.2. Orbital Localization Analysis. The canonical molecular orbital (CMO) usually has strong delocalization, as shown in Figure 2, and the molecular orbital (MO) delocalization is on the whole molecule and cannot well demonstrate the laws of bonding between atoms.[40] To better understand the mechanism of C−O bonding, the Pipek−Mezey localization method was used to transform the CMO into a localized molecular orbital (LMO) through a unitary trans-

formation.[41] Furthermore, the molecular orbitals that contributed to the bonding between atoms were obtained by the MBO occupancy number perturbation method,[42] and visual analysis was carried out in combination with the Visual Molecular Dynamics (VMD) 1.9.3 program. The MBO occupancy number perturbation method can be used to calculate the contribution of each orbital to the MBO, which is helpful to understand the difference in thermal stability between different C−O bonds. The orbitals that have a large contribution to the C−O bond are mainly listed, and the rest can be ignored.

The localized orbital will focus on the characteristics of the most important shared electron pair in the system, as shown in Figure 2. It can be seen from Table 3 that the MBO of the C=O

Table 3. Contribution of the Orbital to the C−O Bond[a]

bond	atom no.	MBO	orbital no.	orbital type	contribution
Ph(C=O)OCH$_3$	36−37	1.952	77	σ	1.004
			91	π	0.668
Ph(CO)−OCH$_3$	36−38	1.116	63	σ	0.863
			109	π	0.256
Ph(CO)O−CH$_3$	38−39	0.904	99	σ	0.906

[a]Ph represents phenyl.

bond in Ph(C=O)OCH$_3$ is 1.952, in which orbital nos. 77 and 91 make major contributions, contributing 1.004 and 0.668 of the MBO, respectively. There is a σ bond and a π bond on atoms 36−37, where the contribution value of the σ bond is 1.004 and so orbital no. 77 is firmly localized on atoms 36−37, and electrons in the orbital were shared by both ends of atoms. For orbital no. 91, the orbitals were not 100% localized on atoms 36−37, and some of them were delocalized on the adjacent 38 O atom. Therefore, the electrons in orbital no. 91 were not shared by atoms 36−37 and their contribution to the C=O bond is not 1.

The MBO of the C−O bond in Ph(CO)−OCH$_3$ is 1.116, which indicates that the chemical bond between atoms 36 and 38 does not only have σ bond but also has certain π bond characteristics. There are obvious characteristics of σ bond between atoms 36 and 38, corresponding to orbital no. 63 but it is not completely firmly localized at atoms 36−38, so the contribution value is only 0.863. Part of no. 63 are delocalized on

atom 37, so the electrons in no. 63 are not completely shared between atoms 36 and 38. The C−O bond of atoms 36−38 has some π bond characteristics, corresponding to orbital no. 109. It can be seen that the delocalization of the π bond is much greater than the π bond in the C=O bond. The orbital no. 109 only partially localized on atoms 36−38, and a part is delocalized to the 37 atoms and appears between atoms 38 and 39, which means that the π bond features between atoms 36 and 38 are much weaker than that of the C=O double bond, resulting in the MBO of the C−O bond in Ph(CO)−OCH$_3$ being much smaller than C=O.

The C−O bond order in Ph(CO)O−CH$_3$ is only 0.904 and the main contribution orbital is no. 99; the contribution value is 0.906, which may be due to a bias caused by the program. It can be seen that there is only one σ bond localized at atoms 38−39, and no π bond LMO was shown. However, part of orbital no. 99 is also delocalized to the 36 C atom, which makes the C−O in Ph(CO)O−CH$_3$ most prone to chemical fracture during HTC. This can be explained as follows: the closer the chemical bond is to the stable structure, the larger the bond order.[35] The distance between the C−O of Ph(CO)O−CH$_3$ and the benzene ring is larger than that between the C−O of Ph(CO)−OCH$_3$ and the benzene ring, resulting in the MBO of the former to be 0.904, while the MBO of the latter is 1.116. Therefore, unstable small molecules are more likely to be removed, and the whole structure tends to form stable aromatic structures in HTC. This also well corresponds to the calculation results of BDE: Ph(CO)−OCH$_3$ has two contribution orbitals, whose dissociation energy is 102.51 kcal/mol, which is 13.57 kcal/mol more than that of Ph(CO)O−CH$_3$ and the stability of the former is also higher during HTC.

Using the analysis of the orbital localization and the MBO analysis method of the occupancy perturbation, it can be found that the σ and π bonds of Ph(C=O)OCH$_3$ are the strongest, and the σ bond contributes 50% of the MBO. The C−O bond in Ph(CO)−OCH$_3$ has slightly stronger σ bond and weaker π bond characteristics. There is only one strong σ bond characteristic in Ph(CO)O−CH$_3$ and so the sequence of chemical bond breakage in Ph(C=O)OCH$_3$ molecules is the C−O bond between atoms 38−39, 36−38, and 36−37 during HTC.

2.3. ESP Analysis. The ESP consists of the contribution from the positive charge of the nucleus and the negative charge of the electron. If the ESP is positive at some point on the molecular surface, it means that the ESP is mainly contributed by the atomic nuclear charge; if negative, it means that the electron makes the main contribution.[43] On the molecular surface, the contribution of electrons and the contribution of the nucleus can be counterbalanced. The uneven distribution of electron density will cause the ESP of the molecular surface to be positive or negative. In common molecular systems, the negative value of ESP usually occurs near lone pair electrons, π electrons, and C−C strong tension bonds of atoms with higher electronegativity because of the density of regional electrons.[44] The isosurface with an electron density of 0.001 e/b3 is usually used as the van der Waals surface of the molecule, and the distribution of ESP on the van der Waals surface of molecules is a common method used to predict the interaction patterns and reaction sites between molecules. There are many oxygen-containing functional groups in lignite and so the most significant noncovalent interactions are mostly hydrogen bonds. The local minima with negative potentials, such as the lone pair of the oxygen atom in the hydroxyl group and ether

bond, can serve as a potential hydrogen bond acceptor, and the hydrogen atom connected to the oxygen atom can usually be used as a hydrogen bond donor. Therefore, it is necessary to construct the molecular surface electrostatic potential of lignite to predict the chemical reaction sites in HTC.

The results of ESP distribution on the van der Waals surface are shown in Figure 3. There are some ESP minimum points
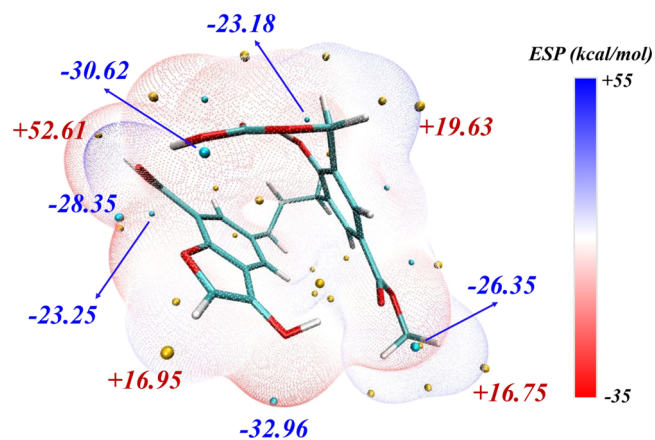

Figure 3. Surface electrostatic potential of lignite molecules.

near the alcohol hydroxyl oxygen of C$_4$H$_5$O−OH, the carbonyl oxygen of Ph−(CO)OCH$_3$, the alcohol hydroxyl oxygen of Ph−(CO)OH, and the phenolic hydroxyl oxygen of Ph−(CO)OH, whose ESP values are −32.96, −26.35, −23.25, and −23.18 kcal/mol, respectively. The strongest electrophilic point occurs near the alcoholic hydroxyl oxygen of C$_4$H$_5$O−OH because the oxygen electronegativity is too strong, leading to hydrogen atoms around the electrons getting attracted to the oxygen. Therefore, the group is most likely to be the preferred reaction site and an electrophilic attack is conducive to interact with water to form hydrogen bonds in HTC. There are two minimum values of −28.35 and −30.62 kcal/mol in the overlap region between the carbonyl oxygen of Ph−(CO)OH and ether-bonded oxygen of C$_4$H$_5$O−OH, and in the overlap region between the alcohol hydroxyl oxygen and the ether-bonded oxygen of CH$_3$−OC(O)OH, respectively. This is because the lone pair electrons of the oxygen atom overlap, resulting in a region with a negative ESP. There are also some local minimum points on both sides of the benzene ring, which may be related to the abundance of unsaturated π electrons in the benzene ring. These ESP regions are not uniformly distributed on the lignite surface and constitute the molecular lignite surface ESP. There are also some areas with positive ESP on the lignite surface, which are mostly distributed near the hydrogen atoms connected with oxygen atoms. This is because the oxygen atoms in these groups generally have strong electronegativity and so the induction effect results in the uneven distribution of electrons. The ESP maximum point is located near the alcohol hydroxyl hydrogen of Ph−(CO)OH, whose ESP value is +52.61. There is a wide range of positive ESP regions near the methyl groups of Ph−(CO)OCH$_3$ and CH$_3$−OC(O)OH, which is caused by the inhomogeneous electron distribution of the methyl group itself.

Figure 4 shows the distribution of the percentage of lignite molecular surface areas with different ESP values. It can be seen that on the lignite surface, the ESP value between −10 and +15 kcal/mol occupies a dominant position, and the ESP near the
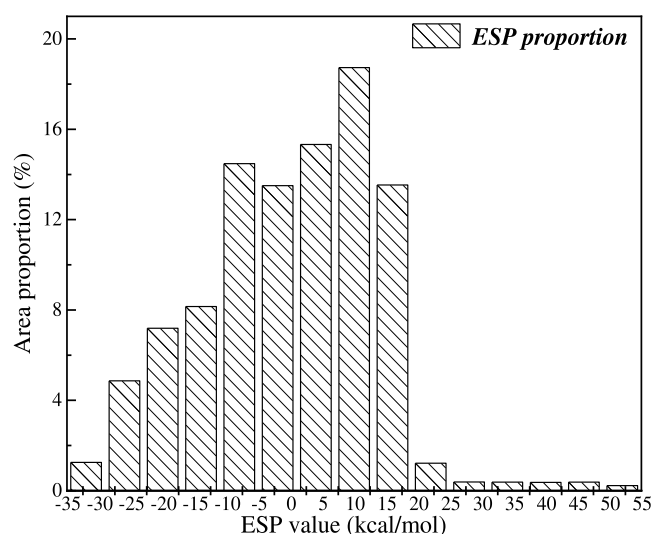
Figure 4. Electrostatic potential distribution of lignite.

oxygen atom in the functional group is mostly less than −20 kcal/mol, while the hydrogen atom on the molecular surface constitutes the region with positive ESP. Therefore, the area near the benzene ring and the aliphatic chain occupies the main position on the surface of ESP.

In summary, there are some local minimum points of ESP in the regions near oxygen functional groups, benzene rings, and aliphatic chains, which are due to the strong electronegativity of oxygen atoms and the unsaturated π electrons in benzene rings. The two points with the strongest electrophilicity are the alcohol

hydroxyl oxygen of C_4H_5O-OH and the overlapping regions of alcohol hydroxyl oxygen and ether-bonded oxygen of $CH_3-OC(O)OH$, which are most likely to weakly interact with water to form hydrogen bonds and can also explain the strong hydrophilicity of lignite.

2.4. Independent Gradient Model (IGM) Analysis. The Multiwfn 3.8 program was used to investigate the weak interaction of the optimized model molecule and the water complex through IGM analysis. Subsequently, the weak interaction between the model molecule and water complexes was visualized using VMD 1.9.3 program. Figure 5a−e shows the isosurface map and scatter plots between the intermolecular density gradients g^{inter} and $\text{sign}(\lambda_2)\rho$ of five model molecule−water complexes. The colors presented by different $\text{sign}(\lambda_2)\rho$ values on the isosurface can be used to identify weak interactions between different types of molecules, and λ_2 can be used to distinguish between bonding ($\lambda_2 > 0$) and nonbonding ($\lambda_2 < 0$). For the area where $\text{sign}(\lambda_2)\rho$ is less than −0.02 au, it is usually reflected in the formation of hydrogen bonds, and the more negative the value of $\text{sign}(\lambda_2)\rho$, the stronger the attraction between molecules.[45] For the area with a value of −0.02 to 0.02 au, it is usually embodied as van der Waals effect. For the area where $\text{sign}(\lambda_2)\rho$ is greater than 0.02 au, it is usually a strong steric effect, and the larger the value, the stronger the steric effect. In the isosurface map, the color range of blue−green−red is used in the range of −0.02 to 0.02 au. According to the $\text{sign}(\lambda_2)\rho$ value, blue represents the formation of hydrogen bonds, green represents van der Waals interaction, and red represents the steric effect. The larger the area of the scatter points on the scatter plot, the higher the density of the scatter
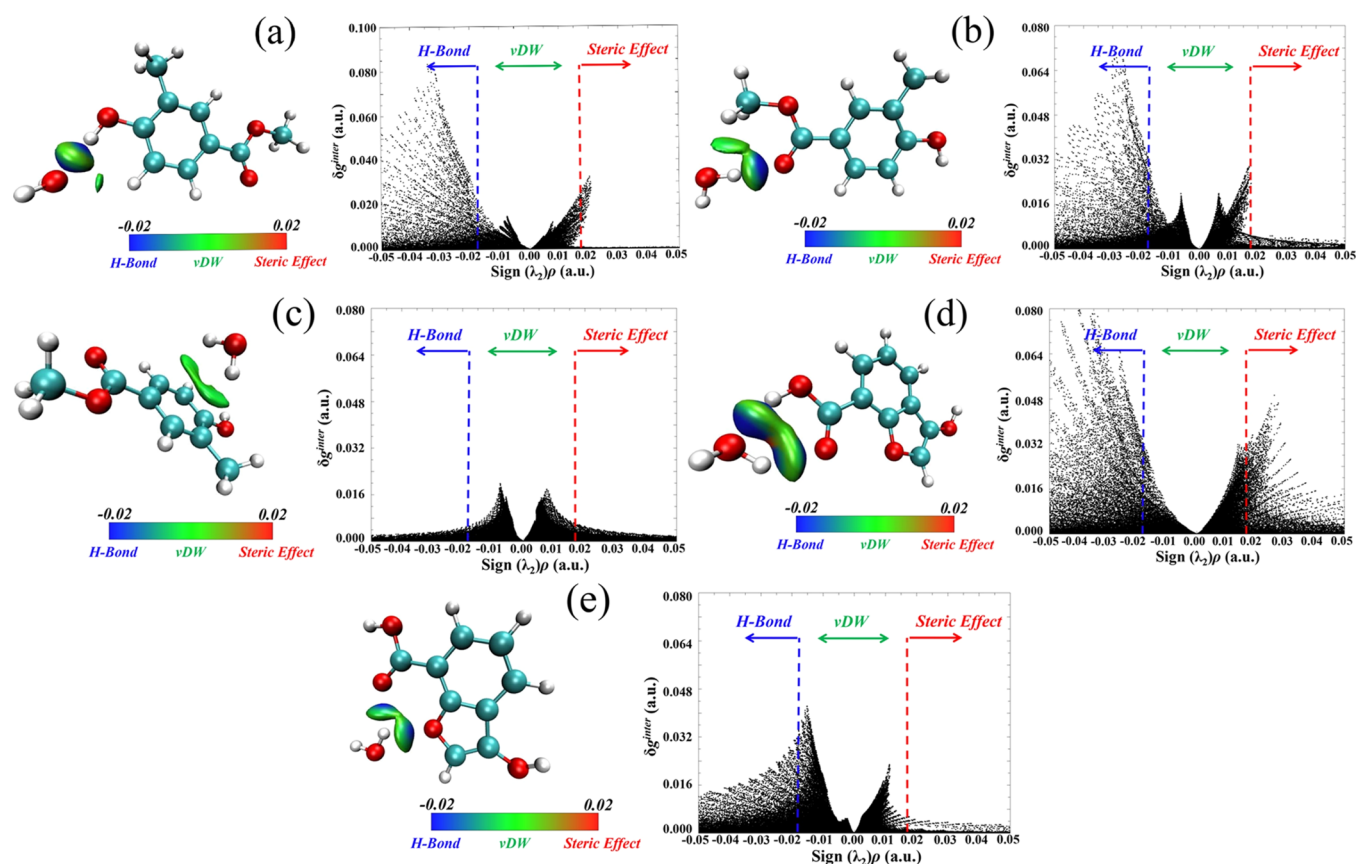

Figure 5. Isosurface and scatter plot: (a) A model, (b) B model, (c) C model, (d) D model, and (e) E model.

points and the stronger the interaction corresponding to the sign(λ_2)ρ value.[46]

As shown in Figure 5a, a typical O···H−O hydrogen bond and van der Waals interaction were formed between the phenolic hydroxyl group and water molecules, which were, respectively, reflected in a relatively concentrated blue region and a large range of green region in the isosurface, in which the phenolic hydroxyl group acts as the donor of hydrogen bonds. These two effects are also shown in the scatter plots, in the area where sign(λ_2)ρ < −0.02 au, a large area of scattered points can be seen. However, between −0.02 and 0.02 au, there are more dense scattered spots and obvious spikes. As seen in Figure 5b, the O−H···O hydrogen bond and van der Waals interaction are formed between water molecules and the carbonyl group and methyl group of the −(CO)OCH$_3$ group. The water molecules act as the donor of hydrogen bonds, which corresponds to the scatter plots showing sign(λ_2)ρ < −0.02 au. In addition, the van der Waals effect of model B is stronger than that of model A. As shown in Figure 5c, a strong van der Waals interaction is formed between the benzene ring and the water molecule, although there would be an O−H···π weak hydrogen bond between the water molecule and the benzene ring; the van der Waals interaction is dominant. It can be seen that there is a large green isosurface between the water molecule and the benzene ring, which corresponds to the area in −0.02 to 0.02 au in the scatter plot. As shown in Figure 5d, when water is adsorbed near the carboxyl group, obvious hydrogen bonding and steric effects can be seen in the isosurface map. The water molecules and the carboxyl groups form two kinds of hydrogen bonds, O−H···O and O···H−O, respectively. The blue regions at both ends of the isosurface are dominant, with red in the middle of the blue. It can be seen from the scatter plots that a large area of scatter exists in the region where sign(λ_2)ρ < −0.02 au, corresponding to hydrogen bonds. In the region where sign(λ_2)ρ > 0.02 au, there are some radioactive scattered points, indicating that a strong steric effect is formed between lignite and water. As seen in Figure 5e, the O−H···O hydrogen bond is formed by the water molecule with the oxygen in the carboxyl group and the oxygen in the furan group, and the water molecule acts as the donor of the hydrogen bond. In addition, it can be seen that the hydrogen bond of model E is weaker than those of models A, B, and D, which can be intuitively reflected in the scatter plots.

The IGM isosurface coloring map is used to describe the weak interactions between water molecules and lignite at different sites in detail. Models A, B, and E formed weak interaction with hydrogen bond as the main force; model E showed the weakest hydrogen bond, while model C showed van der Waals interaction as the dominant force. In addition, some steric effect was also observed in model D.

3. CONCLUSIONS

The molecular model of lignite was constructed, and the removal mechanism of chemical bonds and oxygen-containing functional groups in the process of HTC was studied through DFT calculations at the molecular level. The difference in fragment structures and electronic effects has a great impact on the BDE and bond order. According to results of BDE and bond order, the first group to break in HTC is the methyl of Ph(CO)O−CH$_3$, followed by the C−O of CH$_3$−OC(O)OH; the hydroxyl in Ph−OH is the most thermally stable group, followed by the hydroxyl in CH$_3$OC(O)−OH. In addition, the orbital localization analysis has also been carried out: all three chemical bonds of Ph(CO)OCH$_3$ show the characteristics of σ

bond, while Ph(C=O)OCH$_3$ and Ph(CO)−OCH$_3$ with the MBO >1 also contains certain π bond characteristics. The lignite van der Waals surface ESP was constructed and visualized, and the results showed that oxygen-containing functional groups mainly contributed to the area with a large absolute ESP. According to the IGM analysis, models A, B, and E formed weak interaction with hydrogen bond as the main force; model E showed the weakest hydrogen bond, while model C showed van der Waals interaction as the dominant force. In addition, some steric effect was also observed in model D.

4. METHODS

4.1. Model Construction and Geometry Optimization.
Since there has been no accurate conclusion on the lignite molecular structure, this study was based on the model proposed by Wender[17] and Kumagai et al.[18] and is further constructed using methyl saturation and hydrogen saturation methods. As shown in Figure 6, the model takes benzene ring, furan, and
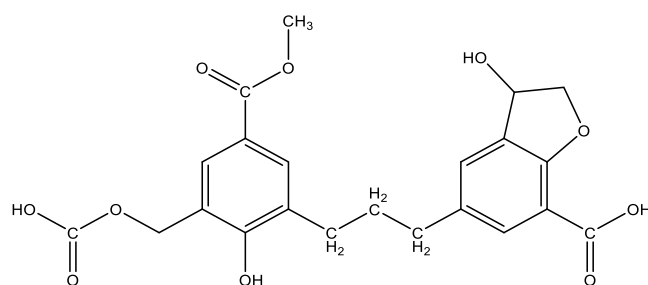

Figure 6. Lignite model constructed in this study.

methylene as a molecular skeleton, and side chains were connected with functional groups such as carboxyl group, carbonyl group, and a hydroxyl group. In addition, to study the weak interaction between functional groups of lignite and water in HTC, five model molecule−water adsorption models were constructed, which were, respectively, labeled as models A, B, C, D, and E (as shown in Figure 7).

In this study, the Gaussian 09[19] program was used to optimize the lignite model and the model molecule−water adsorption model complex. The lignite model was optimized at the B3LYP/6-311G(d,p) level;[20,21] the model molecule−water adsorption model is optimized at the ωB97XD/6-311+G(d,p) level,[22] which has a good effect on the optimization of the weak interaction model.

4.2. Bond Order Analysis.
Bond order is an important analysis method, which can quantitatively express the characteristics of chemical bonds. Two representative bond orders analysis methods were used to analyze lignite molecules via the Multiwfn 3.8[23] program.

4.2.1. Mayer Bond Order (MBO). MBO[24] can reflect the electron logarithm shared between a pair of atoms and is insensitive to the polarity of bonds. For the same kind of chemical bonds, the value of the MBO can reflect the strength, which is defined as

$$\begin{aligned} \text{MBO}_{AB} &= I_{AB}^{\alpha} + I_{AB}^{\beta} \\ &= 2 \sum_{\alpha \in A} \sum_{\alpha \in B} [(P^{\alpha}S)_{ba}(P^{\alpha}S)_{ab} + (P^{\beta}S)_{ba}(P^{\beta}S)_{ab}] \end{aligned}$$

(1)

where P^{α} and P^{β} are the α and β electron density matrices, respectively, and S is the overlapping matrix.
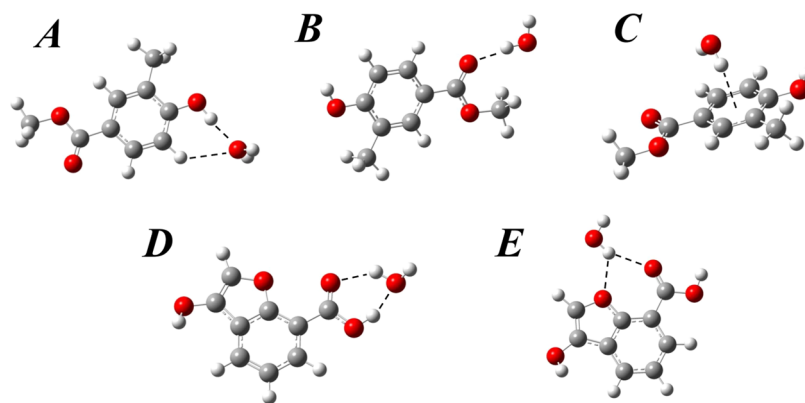
Figure 7. Adsorption sites of different water molecules.

4.2.2. Laplacian Bond Order (LBO).

LBO[25] can measure the polarity of bonds, which is close to the theoretical bond order, and the strength of the bond can be well-reflected. Atoms with greater electronegativity have stronger bond polarity, and the LBO value is smaller. Therefore, the LBO can be considered as the contribution of the covalent part of the bond and is defined as follows

$$\text{LBO}_{A,B} = -10 \times \int_{\nabla^2 \rho < 0} w_A(r) w_B(r) \nabla^2 \rho(r) \, dr \quad (2)$$

where w is the weight function of the smooth change, which represents the fuzzy atomic space; w_A and w_B are the fuzzy overlap spaces corresponding to atoms A and B, respectively; and -10 is the prefactor, which makes the magnitude of the Laplace bond order consistent with common covalent bonds.

4.3. Bond Dissociation Enthalpy (BDE) Analysis.

The BDE can reflect the enthalpy change of chemical bond dissociation in a chemical reaction and is an analytical method to quantitatively reflect the strength of the chemical bond.[26] By calculating the BDE of some C—O bonds and oxygen-containing functional groups, the difficulty degree of lignite molecular chemical bond dissociation during HTC can be characterized. In the same chemical atmosphere, the dissociation of small molecular chemical bonds can well predict the same chemical bonds in macromolecules;[27] so, the lignite molecule was decomposed into five fragments, and the chemical bonds involved are shown in Figure 8. The BDE is defined as

$$D°(A − B) = \Delta H_f°(A^\bullet) + \Delta H_f°(B^\bullet) − \Delta H_f°(AB) \quad (3)$$

where $\Delta H_f°(A^\bullet)$, $\Delta H_f°(B^\bullet)$, and $\Delta H_f°(AB)$ are the enthalpies of radical species A, B, and molecule AB, respectively.

The CBS-QB3 thermodynamic combination method was used to calculate the BDE, which has only a 1.0−1.5 kcal/mol error for calculating the thermodynamic enthalpy.[28]

4.4. Orbital Localization Analysis.

The orbital produced by general quantum chemical calculations is called canonical molecular orbital (CMO), which has strong delocalization and cannot reflect the bonding characteristics between atoms.[29] Orbital localization can transform delocalized orbitals into highly localized orbitals without losing the physical meaning of wave functions, which can well reflect the bonding characteristics.[30] The Multiwfn 3.8 program was used for orbital localization analysis.

4.5. Electrostatic Potential (ESP) Analysis.

ESP describes the potential energy of a unit of positive charge at a position (r) around the molecule, which is defined as[31]
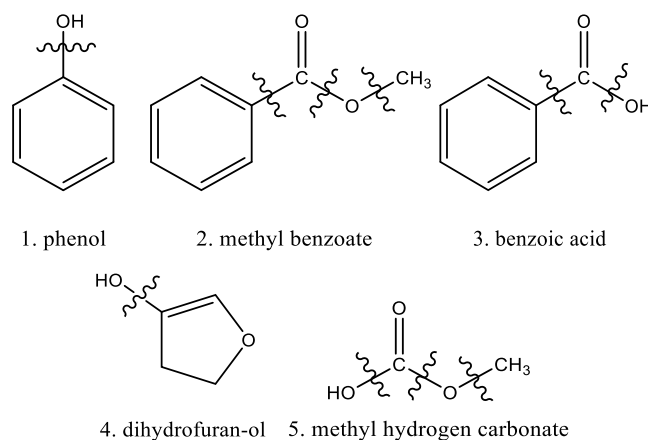

1. phenol   2. methyl benzoate   3. benzoic acid   4. dihydrofuran-ol   5. methyl hydrogen carbonate

Figure 8. Structure of five fragments after decomposition and chemical bond breaking sites.

$$V_{tot}(r) = V_{nuc}(r) + V_{ele}(r) = \sum_A \frac{Z_A}{|r - R_A|} - \int \frac{\rho(r')}{|r - r'|} dr' \quad (4)$$

where V represents the electrostatic potential on the surface of the molecule, Z_A is the nuclear charge located at R_A, and $\rho(r)$ represents the electron density of the molecule. The Multiwfn 3.8 program was used for ESP analysis.

4.6. Independent Gradient Model (IGM) Analysis.

The IGM can show the characteristics of the weak interaction, which can judge whether the interaction between molecules is attractive or repulsive, and characterize the intensity of the interaction,[32] which is defined as

$$g(r) = \left| \sum_i \nabla \rho_i(r) \right| g^{IGM}(r) = \left| \sum_i abs[\nabla \rho_i(r)] \right| \quad (5)$$

$$\delta g(r) = g^{IGM}(r) - g(r) \quad (6)$$

$$g^{inter}(r) = \left| \sum_A \sum_{i \in A} \nabla \rho_i(r) \right| \quad (7)$$

where i is an atomic number, $\nabla \rho_i$ is a gradient vector, $abs \nabla \rho_i$ stands for the absolute value of every component of the $\nabla \rho$ vector inside (still maintaining the vector form), and $| \, |$ represents the modulus of the vector. $g^{inter}(r)$ is the density gradient between molecules. The Multiwfn 3.8 program was used for IGM analysis.

■ AUTHOR INFORMATION

Corresponding Authors

Guangwei Wang − *School of Metallurgical and Ecological Engineering, University of Science and Technology Beijing, Beijing 100083, China;* ⊚ orcid.org/0000-0001-6023-8553; Email: guangwei_wang@ustb.edu.cn

Xiaojun Ning − *School of Metallurgical and Ecological Engineering, University of Science and Technology Beijing, Beijing 100083, China*; Email: ningxj@ustb.edu.cn

Runsheng Xu − *School of Metallurgical and Ecological Engineering, University of Science and Technology Beijing, Beijing 100083, China;* ⊚ orcid.org/0000-0003-2745-6780; Email: xu_runsheng@163.com

Authors

Han Dang − *School of Metallurgical and Ecological Engineering, University of Science and Technology Beijing, Beijing 100083, China*

Chunmei Yu − *School of Metallurgical and Ecological Engineering, University of Science and Technology Beijing, Beijing 100083, China*

Jianliang Zhang − *School of Metallurgical and Ecological Engineering, University of Science and Technology Beijing, Beijing 100083, China*

Nan Zhang − *School of Metallurgical and Ecological Engineering, University of Science and Technology Beijing, Beijing 100083, China*

Yi Gao − *Laboratory for Thermal Science and Power Engineering of MOE, Tsinghua University, Beijing 100084, China*

Chuan Wang − *Swerim AB, SE-971 25 Luleå, Sweden; Thermal and Flow Engineering Laboratory, Åbo Akademi University, Åbo FI-20500, Finland*

Complete contact information is available at:
https://pubs.acs.org/10.1021/acsomega.1c03866

Notes

The authors declare no competing financial interest.

■ REFERENCES

(1) Pauline, A. L.; Joseph, K. Hydrothermal carbonization of organic wastes to carbonaceous solid fuel − A review of mechanisms and process parameters. *Fuel* **2020**, *279*, No. 118472.

(2) Chen, X.; Wang, C.; Wang, Z.; Zhao, H.; Liu, H. Preparation of high concentration coal water slurry of lignite based on surface modification using the second fluid and the second particle. *Fuel* **2019**, *242*, 788−793.

(3) Xiao, K.; Liu, H.; Li, Y.; Yi, L.; Zhang, X.; Hu, H.; Yao, H. Correlations between hydrochar properties and chemical constitution of orange peel waste during hydrothermal carbonization. *Bioresour. Technol.* **2018**, *265*, 432−436.

(4) Evcil, T.; Simsir, H.; Ucar, S.; Tekin, K.; Karagoz, S. Hydrothermal carbonization of lignocellulosic biomass and effects of combined Lewis and Brønsted acid catalysts. *Fuel* **2020**, *279*, No. 118458.

(5) Wang, G.; Qin, X.; Shen, J.; Zhang, Z.; Han, D.; Jiang, C. Quantitative analysis of microscopic structure and gas seepage characteristics of low-rank coal based on CT three-dimensional reconstruction of CT images and fractal theory. *Fuel* **2019**, *256*, No. 115900.

(6) Jin, H.; Fan, C.; Guo, L.; Liu, S.; Cao, C.; Wang, R. Experimental study on hydrogen production by lignite gasification in supercritical water fluidized bed reactor using external recycle of liquid residual. *Energy Convers. Manage.* **2017**, *145*, 214−219.

(7) Mo, J. J.; Xue, Y.; Liu, X. Q.; Qiu, N. X.; Chu, W.; Xie, H. P. Quantum chemical studies on adsorption of CO_2 on nitrogen-containing molecular segment models of coal. *Surf. Sci.* **2013**, *616*, 85−92.

(8) Wu, J.; Wang, J.; Liu, J.; Yang, Y.; Cheng, J.; Wang, Z.; Zhou, J.; Cen, K. Moisture removal mechanism of low-rank coal by hydrothermal dewatering: Physicochemical property analysis and DFT calculation. *Fuel* **2017**, *187*, 242−249.

(9) Liu, J.; Wu, J.; Zhu, J.; Wang, Z.; Zhou, J.; Cen, K. Removal of oxygen functional groups in lignite by hydrothermal dewatering: An experimental and DFT study. *Fuel* **2016**, *178*, 85−92.

(10) Feng, X.; Zhang, C.; Tan, P.; Zhang, X.; Fang, Q.; Chen, G. Experimental study of the physicochemical structure and moisture readsorption characteristics of Zhaotong lignite after hydrothermal and thermal upgrading. *Fuel* **2016**, *185*, 112−121.

(11) Man, C.; Liu, Y.; Zhu, X.; Che, D. Moisture Readsorption Performance of Air-Dried and Hydrothermally Dewatered Lignite. *Energy Fuels* **2014**, *28*, 5023−5030.

(12) Wan, K.; Pudasainee, D.; Kurian, V.; Miao, Z.; Gupta, R. Changes in Physicochemical Properties and the Release of Inorganic Species during Hydrothermal Dewatering of Lignite. *Ind. Eng. Chem. Res.* **2019**, *58*, 13294−13302.

(13) Aziz, M.; Juangsa, F. B.; Kurniawan, W.; Budiman, B. A. Clean Co-production of H_2 and power from low rank coal. *Energy* **2016**, *116*, 489−497.

(14) Ranathunga, A. S.; Perera, M. S. A.; Ranjith, P. G.; Wei, C. H. An experimental investigation of applicability of CO_2 enhanced coal bed methane recovery to low rank coal. *Fuel* **2017**, *189*, 391−399.

(15) Ranathunga, A. S.; Perera, M. S. A.; Ranjith, P. G.; Bui, H. Super-critical CO_2 saturation-induced mechanical property alterations in low rank coal: An experimental study. *J. Supercrit. Fluids* **2016**, *109*, 134−140.

(16) Li, Y.; Zhao, H.; Song, Q.; Wang, X.; Shu, X. Influence of critical moisture content in lignite dried by two methods on its physicochemical properties during oxidation at low temperature. *Fuel* **2018**, *211*, 27−37.

(17) Wender, I. Catalytic Synthesis of Chemicals from Coal. *Catal. Rev.* **1976**, *14*, 97−129.

(18) Kumagai, H.; Chiba, T.; Nakamura, K. Change in physical and chemical characteristics of brown coal along with a progress of moisture release. *Prepr. Pap. − Am. Chem. Soc., Div. Fuel Chem.* **1999**, *44*, 633−636.

(19) Frisch, M. J.; Trucks, G. W.; Schlegel, H. B.; Scuseria, G. E.; Robb, M. A.; Cheeseman, J. R. *Gaussian 09*, revision C. 01; Gaussian, Inc.: Wallingford, CT, 2010.

(20) Stephens, P. J.; Devlin, F. J.; Chabalowski, C. F.; Frisch, M. J. Ab Initio Calculation of Vibrational Absorption and Circular Dichroism Spectra Using Density Functional Force Fields. *J. Phys. Chem. A* **1994**, *98*, 11623−11627.

(21) Andersson, M. P.; Uvdal, P. New Scale Factors for Harmonic Vibrational Frequencies Using the B3LYP Density Functional Method with the Triple-Basis Set 6-311+G(d,p). *J. Phys. Chem. A* **2005**, *109*, 2937−2941.

(22) Al-Jaber, A. S.; Bani-Yaseen, A. D. On the encapsulation of Olsalazine by beta-cyclodextrin: A DFT-based computational and spectroscopic investigations. *Spectrochim. Acta, Part A* **2019**, *214*, 531−536.

(23) Lu, T.; Chen, F. Multiwfn: a multifunctional wavefunction analyzer. *J. Comput. Chem.* **2012**, *33*, 580−592.

(24) Matito, E.; Poater, J.; Solà, M.; Duran, M.; Salvador, P. Comparison of the AIM Delocalization Index and the Mayer and Fuzzy Atom Bond Orders. *J. Phys. Chem. A* **2005**, *109*, 9904−9910.

(25) Lu, T.; Chen, F. Bond order analysis based on the Laplacian of electron density in fuzzy overlap space. *J. Phys. Chem. A* **2013**, *117*, 3100−3108.

(26) Walsh, R. Bond Dissociation Energy Values in Silicon-Containing Compounds and Some of Their Implications. *Acc. Chem. Res.* **1981**, *14*, 246−252.

(27) Vallejo, F.; Díaz-Robles, L. A.; Vega, R.; Cubillos, F. A novel approach for prediction of mass yield and higher calorific value of hydrothermal carbonization by a robust multilinear model and regression trees. *J. Energy Inst.* **2020**, *93*, 1755−1762.

(28) Pokon, E. K.; Liptak, M. D.; Feldgus, S.; Shields, G. C. Comparison of CBS-QB3, CBS-APNO, and G3 Predictions of Gas Phase Deprotonation Data. *J. Phys. Chem. A* **2001**, *105*, 10483−10487.

(29) Wagner, F. R.; Bezugly, V.; Kohout, M.; Grin, Y. Charge decomposition analysis of the electron localizability indicator: a bridge between the orbital and direct space representation of the chemical bond. *Chem. − Eur. J.* **2007**, *13*, 5724−5741.

(30) Aquilante, F.; Pedersen, T. B.; Sanchez de Meras, A.; Koch, H. Fast noniterative orbital localization for large molecules. *J. Chem. Phys.* **2006**, *125*, No. 174101.

(31) Bayly, C. I.; Cieplak, P.; Cornell, W.; Kollman, P. A. A Well-Behaved Electrostatic Potential Based Method Using Charge Restraints for Deriving Atomic Charges: The RESP Model. *J. Phys. Chem. B* **1993**, *97*, 10269−10280.

(32) Nielsen, K. L.; Niordson, C. F. A numerical basis for strain-gradient plasticity theory: Rate-independent and rate-dependent formulations. *J. Mech. Phys. Solids* **2014**, *63*, 113−127.

(33) Cao, B.; Du, J.; Cao, Z.; Sun, H.; Sun, X.; Fu, H. Theoretical study on the alkylation of o-xylene with styrene in $AlCl_3$-ionic liquid catalytic system. *J. Mol. Graphics Modell.* **2017**, *74*, 8−15.

(34) Cao, X.; Cumming, D.; Goh, J.; Wang, X. The impact of investor protection law on global takeovers: LBO vs. non-LBO transactions. *J. Int. Financ. Mark., Inst. Money* **2019**, *59*, 1−18.

(35) Mo, Q.; Liao, J.; Chang, L.; Chaffee, A. L.; Bao, W. Transformation behaviors of C, H, O, N and S in lignite during hydrothermal dewatering process. *Fuel* **2019**, *236*, 228−235.

(36) Mo, Q.; Liao, J.; Chang, L.; Han, Y.; Chaffee, A. L.; Bao, W. Study on combustion performance of hydrothermally dewatered lignite by thermal analysis technique. *Fuel* **2021**, *285*, No. 119217.

(37) Ge, L.; Zhang, Y.; Wang, Z.; Zhou, J.; Cen, K. Effects of microwave irradiation treatment on physicochemical characteristics of Chinese low-rank coals. *Energy Convers. Manage.* **2013**, *71*, 84−91.

(38) Mulder, P.; Korth, H.-G.; Pratt, D. A.; DiLabio, G. A.; et al. Critical Re-evaluation of the O-H Bond Dissociation Enthalpy in Phenol. *J. Phys. Chem. A* **2005**, *109*, 2647−2655.

(39) Yan, M.; Hantoko, D.; Kanchanatip, E.; Zheng, R.; Zhong, Y.; Mubeen, I. Valorization of sewage sludge through catalytic sub- and supercritical water gasification. *J. Energy Inst.* **2020**, *93*, 1419−1427.

(40) Bordwell, F. G.; Liu, W. Z. Solvent Effects on Homolytic Bond Dissociation Energies of Hydroxylic Acids. *J. Am. Chem. Soc.* **1996**, *118*, 10819−10823.

(41) Grimme, S.; Antony, J.; Ehrlich, S.; Krieg, H. A consistent and accurate ab initio parametrization of density functional dispersion correction (DFT-D) for the 94 elements H-Pu. *J. Chem. Phys.* **2010**, *132*, No. 154104.

(42) Feixas, F.; Matito, E.; Duran, M.; Solà, M.; Silvi, B. Electron Localization Function at the Correlated Level: A Natural Orbital Formulation. *J. Chem. Theory Comput.* **2010**, *6*, 2736−2742.

(43) Politzer, P.; Murray, J. S. The fundamental nature and role of the electrostatic potential in atoms and molecules. *Theor. Chem. Acc.* **2002**, *108*, 134−142.

(44) Mulder, P.; Korth, H. G.; Pratt, D. A.; DiLabio, G. A.; et al. Critical Re-evaluation of the O-H Bond Dissociation Enthalpy in Phenol. *J. Phys. Chem. A* **2005**, *109*, 2647−2655.

(45) Saleh, G.; Gatti, C.; Lo Presti, L. Non-covalent interaction via the reduced density gradient: Independent atom model vs experimental multipolar electron densities. *Comput. Theor. Chem.* **2012**, *998*, 148−163.

(46) Laughlin, D. C.; Abella, S. R. Abiotic and biotic factors explain independent gradients of plant community composition in ponderosa pine forests. *Ecol. Modell.* **2007**, *205*, 231−240.